THE JOURNAL OF PHYSICAL CHEMISTRY C

Article

Cite This: J. Phys. Chem. C 2018, 122, 14846−14856

pubs.acs.org/JPCC

Impacts of pH and Intermolecular Interactions on Surface-Enhanced Raman Scattering Chemical Enhancements

Hoa T. Phan and Amanda J. Haes*

Department of Chemistry, University of Iowa, Iowa City, Iowa 52242, United States

Supporting Information

ABSTRACT: Surface-enhanced Raman scattering (SERS) is a surface sensitive technique that reveals information regarding molecular adsorption driving forces at nanoparticles surfaces. While the plasmonic properties of SERS substrates provide the largest signal enhancements, chemical enhancement mechanisms are more sensitive to molecular adsorption and intermolecular interactions. Herein, gold coated silver nanoparticles that are stabilized inside microporous silica membranes are used for monitoring short-range chemical enhancement effects. First, the silica membrane provides plasmonic stability while also facilitating kinetic measurements so that impacts of molecular protonation, molecule−molecule interactions, molecule−silica interactions, and molecule−Au interactions can be identified. To do this, the vibrational frequencies of 4-mercaptobenzoic acid (4-MBA) are monitored as a function of time and pH. Applying Fick's second law to time-dependent responses reveals that molecular flux decreases with increasing pH. SERS spectra suggest that the kinetics of this phenomenon depend on the protonation state of 4-MBA and, hence, the energy required for the molecules to pass through the negatively charged silica membrane. Namely, repulsive electrostatic interactions between deprotonated molecules ($R\text{-}COO^-$) and the silica shell increase the energy required for transport, which subsequently decreases the flux of molecules through the silica shell and subsequent adsorption to the metal surface. As pH approaches neutral conditions, the fraction of deprotonated 4-MBA increases. These molecules, which have a higher electron density in the aromatic rings versus protonated ones, favor selective chemical enhancement of the asymmetric versus symmetric C−C stretching modes. In addition, increasing intermolecular interactions between adsorbed molecules promote electron delocalization from aromatic rings to the carboxylate groups of 4-MBA. This response causes the pK_a of the carboxylate to gradually increase from 4.8 (in solution) to 7.7 (on nanoparticle surfaces). Consequently, SERS signals for this molecule can be understood with respect to molecular protonation state, flux, and intermolecular interactions using these electromagnetically stable plasmonic nanostructures.

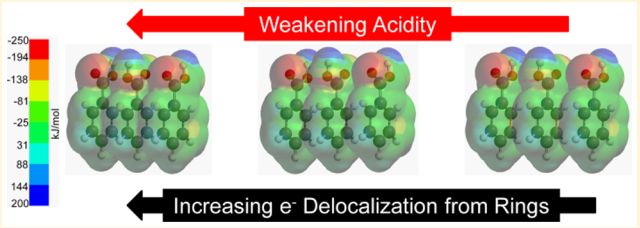

INTRODUCTION

Surface-enhanced Raman scattering (SERS) is a highly sensitive technique that can be used to detect trace amounts of target molecules based on enhanced signals of vibrational modes using plasmonic nanoparticles.[1−4] Critical to these studies is successful molecular flux to an interface so that the residence time of the molecules is long enough to facilitate detection.[5−7] Molecules with a strong affinity (i.e., adsorption) to SERS substrates exhibit extended residence times at the interface,[7] so the kinetics of detection depends on intermolecular interaction energetics (in solution versus on surfaces) and mass transport to the metal surface.[8,9] Previous theoretical studies used continuum[10−12] and discrete stochastic[13,14] models to investigate the impact of intermolecular forces on molecular diffusion process in nanochannels. In the continuum model, molecular flux through a nanochannel is treated as a one-dimension diffusion process, and molecules are assumed to interact with pores uniformly. This model revealed that the flux of molecules with a high affinity to the pores increased when the amount of molecules with weak affinity to the pores increased.[12,15] This finding is in contrast to discrete stochastic model predictions where nanochannels are divided into a series of positively or negatively charged binding sites, which could be used to model repulsive or attractive traps.[8,13] In this model, repulsive barriers at the entry of a pore exhibited a larger forward flux versus an attractive barrier at the same point, which depended on molecular concentration and energetics. Low molecular concentration outside the channels generated a large flux because of the dominance of repulsive traps, while high external molecular concentration promoted transport because of the generation of attractive traps.[14] These theoretical predictions were in a good agreement with experimental studies in biological systems.[16−19]

These same energetic considerations are important in SERS studies as molecular flux to a metallic substrate depends on intermolecular interactions between ions, the target molecule, surface chemistry, and solvent.[20−22] For instance, the chemisorption and SERS activity of 4′-(pyridin-4-yl)-

Received: April 30, 2018
Revised: June 7, 2018
Published: June 8, 2018

DOI: 10.1021/acs.jpcc.8b04019
J. Phys. Chem. C 2018, 122, 14846−14856

biphenyl-4-yl)-methanethiol (4-PBT) on Au(111) were shown to depend on molecular packing density and orientation.[23] After Au−S bond formation, $\pi-\pi$ stacking between adjacent molecules caused the monolayer density to increase over the course of 6 h. These stabilizing interactions were balanced by repulsive dipole−dipole interactions. Monolayer formation and restructuring also influenced the electron density in functional groups thus causing variations in pK_a value. Carboxylic acid groups were shown to weaken in acidity by 1−3 pH units when alkanethiols were adsorbed into ordered monolayers on metallic surfaces versus in solution.[24] The same phenomenon was also observed previously[25−28] when the acidity of carboxylic acid groups of 4-MBA weakened upon adsorption to nanoparticles; however, the impact of intermolecular interactions and electron density were not evaluated.

Intermolecular interactions also influence the electromagnetic enhancement of molecules via surface selection rules[4,23,29,30] and chemical enhancement mechanisms.[23,31] Of importance to the present study, intermolecular interactions can influence electron distribution in molecules thus impacting the modest yet important effect of chemical enhancement on SERS spectra. The most common chemical enhancement occurs via charge transfer[32,33] where the excitation wavelength is in resonance with electronic transitions between either (1) the Fermi level of the metal to the lowest unoccupied molecular orbital or (2) the highest occupied molecular orbital to the Fermi level of the metal.[34,35] Symmetric vibrational modes were shown to be more sensitive to electromagnetic changes, while asymmetric vibrational modes were most dependent on chemical enhancements.[32] These effects were further supported through a series of SERS studies where symmetric and asymmetric vibrational modes were evaluated.[23,31,36]

Herein, the implications of pH and monolayer equilibration time on SERS spectral features associated with 4-MBA are evaluated using internally etched silica-stabilized, gold-coated silver (IE Ag@Au@SiO_2) nanoparticles. The sequential importance of molecular protonation on molecular diffusion through microporous silica membranes, molecular flux, and adsorption on the metal interface, and intermolecular interactions of molecules once formed into a monolayer are investigated using time-dependent localized surface plasmon resonance (LSPR) and SERS spectroscopies. SERS bands associated with the number of molecules as well as those associated with either chemical or electromagnetic enhancements are evaluated using these electromagnetically stable nanostructures. Consequently, important and significant changes in chemical enhancement signatures are understood and related to two commonly varied experimental parameters, pH and equilibration time.

METHODS AND MATERIALS

Chemical Reagents. Gold(III) chloride trihydrate, sodium citrate dihydrate, Amberlite MB-150 mixed bed exchange resin, (3-aminopropyl) trimethoxysilane (APTMS), sodium nitrate ($NaNO_3$), sodium trisilicate (27%), tetraethyl orthosilicate (TEOS), silver perchlorate, sodium borohydride, 4-mercaptobenzoic acid (4-MBA), hydroxylamine hydrochloride, and potassium phosphate dibasic trihydrate ($K_2HPO_4{\cdot}3H_2O$) were purchased from Sigma. Ethanol, ammonium hydroxide (NH_4OH), hydrochloric acid (HCl), nitric acid (HNO_3), and potassium phosphate monobasic (KH_2PO_4) were purchased from Fisher Scientific (Pittsburgh, PA). Ultrapure water (18.2 M$\Omega{\cdot}cm^{-1}$) was obtained from a Barnstead Nanopure System and used for all experiments. All glassware was cleaned with aqua regia (3:1 HCl/HNO_3) and rinsed thoroughly with water before oven (glass) or air (plastic) drying.

Nanoparticle Synthesis. Ag@Au nanoparticles were synthesized using a seeded growth method previously described in the literature.[37,38] Briefly, 99.8 mL of a 300 μM sodium citrate solution prepared in N_2-purged water was stirred in an ice bath in the dark. A 1 M freshly prepared sodium borohydride (100 μL) solution was added to the citrate solution (1 mM final concentration). Next, 100 μL of 100 mM silver perchlorate was added to the solution within 2 min after sodium borohydride addition. The resulting Ag nanoparticle solution was stirred for 3 min. Stirring was then stopped, and Ag nanoparticles with average diameters of 12.2 ± 5.6 nm (N = 353) formed as determined using transmission electron microscopy (TEM). Ag nanoparticle concentration was determined using a previously published molar extinction coefficient for 12.2 nm diameter Ag nanoparticles (3.51×10^9 $M^{-1}{\cdot}cm^{-1}$).[39]

Next, Ag@Au nanoparticles were synthesized by adding 14.1 mL of water to 45 mL of the as-synthesized Ag seeds. This solution was stirred for ∼2 min at 4 °C; then 30.4 mL of both 6.25 mM hydroxylamine hydrochloride and 0.465 mM gold salt was added slowly (3 mL/min) using a syringe pump. This solution was stirred for 1 h then stored at 2−4 °C for 12−18 h to ensure nanoparticle formation. The Ag@Au nanoparticles were triply centrifuged with water (30 min, 2000 × g) and redispersed in a 1 mM citrate solution so that the final nanoparticle concentration was 0.28 nM, which was estimated using a standard estimation model for the silver seeds.[39] An average Ag@Au nanoparticle diameter of 20.6 ± 5.8 nm (N = 461) was determined using TEM.

Silica-coated Ag@Au (Ag@Au@SiO_2) nanoparticles were synthesized via a modified Stöber method.[40−42] The pH and conductivity of 40 mL of the as-synthesized Ag@Au nanoparticles were adjusted to 5 and ∼110 μS/cm using NaOH and Amberlite resin, respectively. After resin removal by filtration, 28 μL of 1 mM freshly prepared APTMS was added dropwise to the nanoparticle solution with stirring. After 30 min, 325 μL of 2.7% sodium silicate was added dropwise to the solution and stirred for 24 h. The silica shell thickness was further increased by adding ethanol (final ratio = 1:4 H_2O/ethanol). After 6 h, 32 μL of 1 mM APTMS and 32 μL of TEOS were added. Next, 160 μL of concentrated NH_4OH was added to increase the pH to ∼11. After 16 h, the Ag@Au@SiO_2 nanoparticles were centrifuged (45 min, 9383 × g) three times with ethanol then three times with water. The Ag@Au@SiO_2 nanoparticles were then passed through a Sephadex-50 column to remove Ag@Au nanoparticles that did not contain complete silica shells[43] and were stored in 100% ethanol until use. Ag@Au@SiO_2 nanoparticles exhibited average overall diameters of 85.5 ± 7.0 nm (N = 193). The average silica shell thickness was 32.5 ± 4.5 nm (propagated error).

Internal Etching. Silica shells were converted into silica membranes via an internal silica etching process induced with concentrated NH_4OH.[2,4,40] Ag@Au@SiO_2 nanoparticles stored in ethanol were triply centrifuged (20 min, 7607 × g) and redispersed in water to 3 nM prior to etching. To obtain an etching profile, nanoparticles were diluted with water in disposable methacrylate cuvettes (optical density was ∼1.5); then concentrated NH_4OH was added so that the final base

DOI: 10.1021/acs.jpcc.8b04019
J. Phys. Chem. C 2018, 122, 14846−14856

concentration was 1.5 M. Once the extinction maximum wavelength (λ_{max}) reached 571.5 nm, the etching reaction was quenched by adding 100 mM HNO_3 so that the solution pH dropped below 4. These internally etched Ag@Au@SiO_2 (IE Ag@Au@SiO_2) nanoparticle solutions were immediately washed 3 times in water by centrifugation (7 min, 7607 × g for the first wash and 15 min, 7607 × g for the second and third washes) and passed through a Sephadex-G50 column to remove uncoated or partially silica coated nanoparticles. IE Ag@Au@SiO_2 nanoparticles were used immediately or stored in 100% ethanol until use.

Phosphate Buffer Preparation. K_2HPO_4 and KH_2PO_4 were mixed to obtain 100 mM phosphate buffer stock solutions with pH values ranging from 6.0 to 7.6. These solutions were diluted in water to a final phosphate concentration of 10 mM. Next, small amounts of HNO_3 were added to slightly adjust pH to desired values. Buffer conductivity was measured using an EC 400 ExStik conductivity/TDS/salinity meter (Extech Instruments, MA) and maintained at 4 mS/cm using 1 M $NaNO_3$.

TEM. TEM was performed using a JEOL JEM-1230 microscope equipped with a Gatan CCD camera. Samples were prepared on 400 mesh copper grids that were coated with a thin film of Formvar and carbon (Ted Pella). The nanoparticle solution was diluted to 50% ethanol, and ∼10 μL was pipetted onto a grid then dried at room temperature. At least 200 nanoparticles were analyzed (Image Pro Analyzer) to estimate average nanoparticle diameters. Silica shell thicknesses were determined by propagation of error between Ag@Au and Ag@Au@SiO_2 nanoparticle diameters.

Electrophoretic Mobility. Ag@Au@SiO_2 nanoparticles were dispersed in 10 mM phosphate buffer to a final concentration of 0.11 nM. Mixtures were transferred to Malvern folded capillary cells for electrophoretic mobility measurements using a Zetasizer Nano-ZS (Malvern Instruments, Westborough, MA). Electrophoretic mobility was converted into ζ potential using Henry's equation:[44,45] $u_e = \frac{2}{3}\frac{\varepsilon_r\varepsilon_o}{\eta} f(\kappa\alpha)\zeta$ where u_e is the electrophoretic mobility ($cm^2 \cdot V^{-1} \cdot s^{-1}$), η is dynamic viscosity ($N \cdot s \cdot m^{-2}$), ε_r and ε_0 are a relative permittivity of the electrolyte and electric permittivity of vacuum, $f(\kappa\alpha)$ is the Henry function, and ζ is ζ potential (V). $pH_{surface}$ was calculated using Gouy−Chapman−Stern theory[46] where $pH_{surface} = pH_{solution} + \frac{e}{2.3k_BT}\zeta$ ($pH_{solution}$ represents the bulk pH of the solution, k_B is the Boltzmann constant, and T is temperature).

Extinction and SERS Spectroscopies. LSPR spectra of Ag nanoparticles were collected using quartz cuvettes (path length = 1 cm) from 200 to 800 nm, and LSPR spectra of Ag@Au and Ag@Au@SiO_2 nanoparticles were collected in methacrylate cuvettes (path length = 1 cm) from 380 to 1000 nm using an ultraviolet−visible (UV−vis) spectrometer (i-trometer BWTek). Deuterium and halogen lamps were used for UV and visible excitation, respectively. LSPR spectra were collected in transmission geometry every 10 s for 45 min (integration time (t_{int}) = 25 ms, average = 25 scans, boxcar = 5). Extinction maximum wavelengths (λ_{max}) were determined from the zero-point crossing of first derivative spectra.

The characteristic electromagnetic field decay length (l_d) for Ag@Au nanoparticles was determined using LSPR and the following model:[47]

$$\Delta\lambda_{max} = m_1(n_{silica} - n_{water})(1 - e^{-2t/l_d}) - m_2[(n_{silica} - n_{water})(1 - e^{-2t/l_d})]^2 \quad (1)$$

where $\Delta\lambda_{max}$ is the LSPR wavelength shift, m_1 is the linear refractive index sensitivity, m_2 is a nonlinear refractive index sensitivity term that accounts for nonlinearity in the local electric field, n_{silica} and n_{water} are the effective refractive indices of silica and the bulk solution, respectively, and t is the silica membrane thickness. To determine these values, Ag@Au and Ag@Au@SiO_2 nanoparticles were incubated in 0−60% (w/v) sucrose solutions,[48] and LSPR spectra were collected. The intersection of these responses was used to estimate the effective refractive index of silica (1.45(6)). The linear and nonlinear refractive index sensitivities were determined to be 146 nm/RIU and 395 nm/RIU^2, respectively. Finally, the l_d for Ag@Au nanoparticles was estimated at ∼11 nm. All of these values are reasonable based on previously published findings.[2,4,47]

SERS measurements were performed using 0.3 nM IE Ag@Au@SiO_2 nanoparticles prepared in 10 mM phosphate buffer (pH 4.5−7.5) and 10 μM 4-MBA. Samples were vortexed for 10 s; then spectra were collected continuously for 45 min using an ExamineR spectrometer (DeltaNu) with an excitation wavelength (λ_{ex}) of 785 nm, laser power (P) = 59 mW, and integration time (t_{int}) = 10 s. Deconvolution of overlapping (i.e., the symmetric and asymmetric C−C stretching mode) vibrational bands was achieved using Gaussian function fitting. To do this, vibrational band centers were evaluated using second derivative analysis, and vibrational bands with positive areas, intensities with S/N greater than 3, and widths greater than 8 cm^{-1} were considered significant. Control spectra (IE Ag@Au@SiO_2 nanoparticles dispersed in buffer) were collected then subtracted from 4-MBA containing samples.

Electron Density Simulations. To determine how electron distribution changes as a function of separation distance, electrostatic potential energies were calculated for the oxygen atom and acidic proton in three energy minimized protonated benzoic acid molecules in water as a function of intermolecular constrained distances ranging from 0.33 to 0.42 nm. This separation range was previously determined to be reasonable for similar molecules.[49−51] Energy was minimized using molecular mechanics theory and the Merck molecular force field (Spartan '10). Molecular angles were constrained to maintain a parallel geometry among the three aromatic rings. Electron density calculations were performed to generate 3D electrostatic potential maps.

RESULTS AND DISCUSSION

Evaluation of How Molecular Diffusion Rates Impact the Density of Adsorbed Molecules on Metal Surfaces. Plasmonic nanoparticles encapsulated in microporous silica membranes were previously shown to promote reproducible and quantitative SERS detection of thiolated molecules when the silica membrane plus void space distance to the metal surface was greater than the 1/e decay length.[2,4,47] Here, we build on those studies using similar electromagnetically isolated Ag@Au nanoparticles with ∼11 nm decay lengths. As shown in Figure 1A, these IE Ag@Au@SiO_2 nanoparticles exhibit an average metal core diameter of 20.6 ± 5.8 nm (N = 461). Upon silica coating and etching, these plasmonic materials are encapsulated by 32.5 ± 4.5 nm (14% relative standard deviation) thick silica + void space. Silica shell

DOI: 10.1021/acs.jpcc.8b04019
J. Phys. Chem. C 2018, 122, 14846−14856

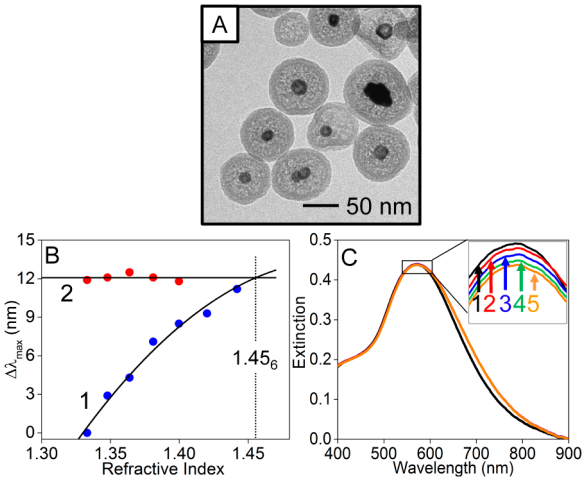

Figure 1. (A) TEM image of IE Ag@Au@SiO_2 nanoparticles. The average diameter is 85.5 ± 7.0 nm (N = 193), and the silica membrane thickness is 32.5 ± 4.5 nm. (B) Bulk refractive index was modified using 0−80% (w/v) sucrose and Ag@Au nanoparticles (1) without and (2) with silica membranes. The data are analyzed using eq 1. The refractive index of silica is estimated to be 1.45(6). (C) LSPR spectra of 0.3 nM IE Ag@Au@SiO_2 nanoparticles (1) before and after incubating with 10 μM 4-MBA in pH 4.5 buffer for (2) 1, (3) 10, (4) 30, and (5) 45 min.

thicknesses on individual particles differed by 4% (±0.8 to ±2.1 nm) indicating relatively good uniformity of silica encapsulation on each structure. By immersing Ag@Au and Ag@Au@SiO_2 nanoparticles in varying sucrose concentrations and monitoring the λ_{max} (Figure 1B-1 and -2, respectively),[48] we estimated the thickness of the silica membrane and void space to be ∼3 times larger than the electromagnetic field decay length, thus providing plasmonic stability of the metal cores as demonstrated in Figure 1C. These representative LSPR spectra show that the spectral line shape, full width at half-maximum (246.4 ± 0.7 nm), and optical density (0.47 ± 0.01) of 0.3 nM IE Ag@Au@SiO_2 nanoparticles do not vary significantly upon incubation in 4-MBA (pH 4.5). Signals remain stable for the course of the experiments, and similar responses are observed in all buffer solutions (pH 4.5−7.5). Thus, the ensemble averaged electromagnetic properties of these materials are considered to be stable throughout all subsequent and concurrent measurements.

Molecular diffusion and flux toward an interface directly impact the local refractive index near the metal surface and, as a result, the extinction maximum wavelength (λ_{max}) in LSPR spectra. Figure 2A shows that the λ_{max} increases then saturates in all studied pH solutions as a function of time consistent with the dielectric sensitivity of plasmonic nanostructures to their local environment until surface saturation occurs or equilibrium is reached. It should be noted that the wavelength range shown in this figure is 6.5 nm relative to the 500 nm wavelength range shown in Figure 1C. This allows us to highlight the small wavelength changes that arise from local refractive index variations near the metal surface. Several differences are noted in the data collected at varying pH including the rate of signal change and saturated λ_{max} values. To quantify time dependent changes and to understand diffusion, effective diffusion coefficients (D_{eff}) of molecules passing through silica membranes are estimated at each pH.

Non-steady-state conditions apply, so molecular diffusion through silica membranes is modeled using Fick's second law of diffusion where changes in molecular concentration at a

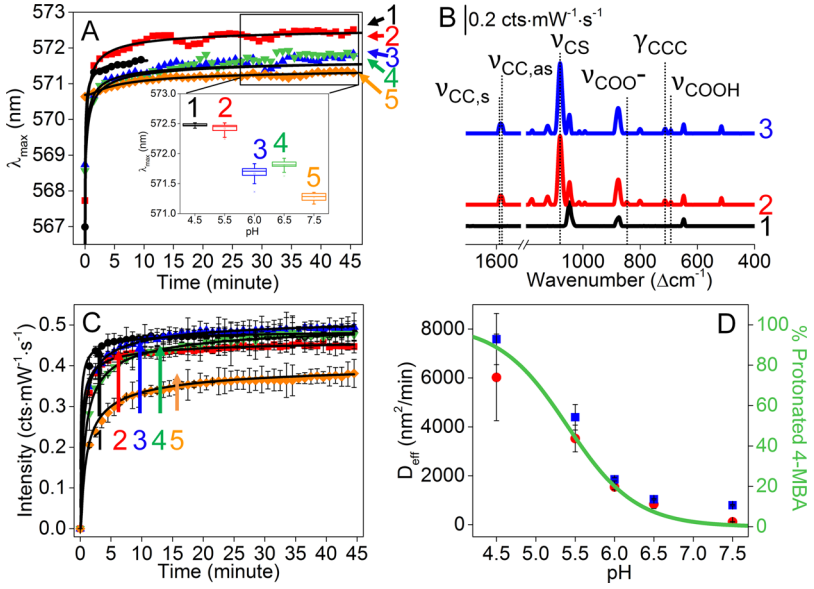

Figure 2. (A) Time-dependent λ_{max} using 0.3 nM IE Ag@Au@SiO_2 nanoparticles in pH (1) 4.5, (2) 5.5, (3) 6.0, (4) 6.5, and (5) 7.5 buffer after the addition of 10 μM 4-MBA. Data are fit using Fick's second law of diffusion. The inset in panel A shows trends in λ_{max} for data collected after 30 min. (B) SERS spectra (1) before and after addition of 10 μM 4-MBA at pH 4.5 for (2) 15 and (3) 30 min. Vibrational modes of 4-MBA are COOH stretching (ν_{COOH}, 693 cm^{-1}), CCC bending (γ_{CCC}, 713 cm^{-1}), COO^- stretching (ν_{COO^-}, 848 cm^{-1}), C−S stretching (ν_{CS}, 1080 cm^{-1}), asymmetric C−C stretching ($\nu_{CC,as}$, 1582 cm^{-1}), and symmetric C−C stretching ($\nu_{CC,s}$, 1592 cm^{-1}). Experimental conditions: λ_{ex}= 785 nm, t_{int}= 10 s, P = 59 mW, averages = 30. (C) Time-dependent SERS intensity of the C−S stretch using the same conditions and fitting as in panel A. (D) Calculated effective diffusion coefficients of 4-MBA as a function of pH from (red) λ_{max} and (blue) C−S stretching intensity data. Percentage of protonated 4-MBA molecules on surfaces of silica membranes (solid line) using the Henderson−Hasselbalch equation assuming a pK_a for 4-MBA = 5.4.

DOI: 10.1021/acs.jpcc.8b04019
J. Phys. Chem. C 2018, 122, 14846−14856

given position (x) that changes with time $\left(\frac{\partial C}{\partial t}\right)$ is equal to the product of the effective diffusion coefficient (D_{eff}) and the second derivative of the concentration gradient $\left(\frac{\partial^2 C}{\partial x^2}\right)$. D_{eff}, which we estimate using the sum of the product of fraction of protonated molecules in solution (ϕ), the diffusion coefficient of the protonated molecules (D_{COOH}), the product of the fraction of deprotonated molecules ($1 - \phi$), and the diffusion coefficient of the deprotonated molecules (D_{COO^-}) through the silica membrane, is related to the total flux of protonated and deprotonated molecules through the silica membrane assuming rapid adsorption upon transport.[52,53] As such, Fick's second law reduces to the following expression:[54]

$$\frac{C_{x,t} - C_0}{C_s - C_0} = 1 - \mathrm{erf}\left(\frac{x}{2\sqrt{D_{eff}t}}\right) \quad (2)$$

where $C_{x,t}$ is the molecular concentration at position x at time t, C_s is the initial concentration of molecules at the entrance of the membrane, and C_0 is the initial concentration of molecules inside the membrane. Initially, C_0 is 0, so Fick's second law (eq 1) reduces to

$$\frac{C_t}{C_s} = 1 - \mathrm{erf}\left(\frac{x}{2\sqrt{D_{eff}t}}\right) \quad (3)$$

By assuming that $\frac{C_t}{C_s}$ is proportional to changes in the time-dependent λ_{max} values, we can estimate D_{eff}. Here, only data collected during the first 10 min are used for this purpose because monolayer restructuring and molecular protonation state occur at longer times (*vide infra*). This reveals that the effective diffusion coefficient of 4-MBA decreases from 6023 to 113 $nm^2 \cdot min^{-1}$ as pH increases from 4.5 to 7.5. This phenomenon can be understood in terms of the average energy required for (i.e., energy barrier that must be overcome) and relative fractions of protonated and deprotonated molecules available to pass through the silica membrane. The driving forces and energetics depend on intermolecular interactions between 4-MBA in solution (ion−dipole),[29] near or in the negatively charged silica membrane (ion−dipole or ion−ion for protonated and deprotonated 4-MBA, respectively),[8,13] and at the gold interface[23] (chemisorption to form Au−S bonds, ∼40 kcal/mol[55−57]). Of note, the observed D_{eff} for protonated 4-MBA through the microporous silica membrane is ∼6000 $nm^2 \cdot min^{-1}$, a value ∼7 orders of magnitude smaller than the solution value ($\sim 10^{10}$ $nm^2 \cdot min^{-1}$).[58] This difference can be understood in terms of the impact of confined space on diffusion as demonstrated previously for rhodamine 6G,[59] metal complexes ($Fe(CN)_6^{3-}$ and $Ru(NH_3)_6^{3+}$),[60] and *n*-heptane[61] where diffusion coefficients were reduced by 5−8 orders of magnitude in silica nanochannels versus in solution.

In addition, molecular protonation state is also expected to impact transport as ion−dipole interactions between protonated 4-MBA and silica are energetically more favorable than the ion−ion repulsive interactions between deprotonated molecules and silica. Thus, there is a greater energy cost for deprotonated molecules to enter and pass through the microporous silica membrane into the void space than for protonated species. This relative energy barrier difference can be quantified as a function of pH relative to that at pH 4.5 using the Eyring equation as follows:[54,62]

$$\Delta\text{Energy Barrier} = k_B T \ln\left(\frac{D_0}{D_{eff}}\right) \quad (4)$$

where D_0 is a proportionality constant (m^2/s). As pH increases from 5.5 to 7.5, this relative energy barrier increases from 0.5 ± 0.3 to 4.0 ± 0.3 $(k_B T)^{-1}$. This suggests that molecular flux through the microporous silica influences the local molecular environment near the metal.

These effects are also observed in corresponding SERS measurements as a function of both time and pH. Figure 2B shows representative SERS spectra of 4-MBA measured using nanoparticles suspended in a pH 4.5 buffer after incubation times of 15 and 30 min. Before 4-MBA addition, only vibrational frequencies consistent with residual silica on the gold surface including SiO_3^- stretching (ν_{SiO_3}, 650 cm^{-1}),[63−65] CCC bending (β_{CCC}, 874 cm^{-1}),[66,67] and C−N stretching (ν_{CN}, 1048 cm^{-1})[68−70] are observed. After 4-MBA addition, the only significant vibrational frequencies observed are consistent with protonated molecules including the COOH stretching (ν_{COOH}, 693 cm^{-1}),[31,36] out-of-plane CCC bending (γ_{CCC}, 713 cm^{-1}),[31,71,72] COO^- stretching (ν_{COO^-}, 840 cm^{-1}),[71−73] C−S stretching (ν_{CS}, 1080 cm^{-1}),[2,71,72] asymmetric C−C stretching ($\nu_{CC,as}$, 1582 cm^{-1}),[31,74] and symmetric C−C stretching ($\nu_{CC,s}$, 1592 cm^{-1})[2,31,71,74] bands.

To quantify D_{eff} as a function of time and pH, the C−S stretching mode intensity, which is directly proportional to the amount of adsorbed 4-MBA and least influenced by molecular orientation,[2,4,36,72] is plotted in Figure 2C. Fitting these data using Fick's second law of diffusion and the Eyring equation reveals that D_{eff} increases from 794 to 7588 $nm^2 \cdot min^{-1}$ while the change in relative energy barrier decreases from 2.3 ± 0.1 to 0.6 ± 0.2 $(k_B T)^{-1}$ as pH decreases. These results are consistent with the local dielectric constant changes estimated from LSPR spectral analysis. This suggests that adsorption to gold occurs quickly once molecules have entered the void space inside the composite nanostructures.

It is well-established that pH impacts molecular protonation in solution and the electrostatic potential of silica.[75,76] When the pH of a solution is between 4.5 and 7.5, the composite nanoparticles used in this study exhibit an average ζ potential of −33.6 ± 10.9 mV, which arises from negatively charged silica, a value that is consistent with previous measurements for similar materials, which averaged −46.6 ± 6.3 mV.[76−78] Another important point is that Gouy−Chapman−Stern theory[46] predicts that the pH near a silica interface is ∼0.6 pH units lower than in solution because of Columbic forces between negatively charged silica and positively charge protons in aqueous solution.

If we assume a similar effect near the silica membranes surrounding the plasmonic nanoparticles in this study, the fraction of protonated 4-MBA molecules near silica membranes would be larger than that in solution thereby causing the effective pK_a of 4-MBA to be ∼5.4 versus the solution value of 4.79.[79,80] This phenomenon is supported in Figure 2D where pH-dependent trends in the effective diffusion coefficients and fraction of protonated 4-MBA molecules in solution predicted using the Henderson−Hasselbalch equation with a pK_a of 5.4 are correlated for 4-MBA. While uncertainty in these values arises from variations in silica shell thickness on individual nanoparticles and among nanoparticles, significant pH dependent responses are noted. This suggests that molecular diffusion near the metal surface is pH-tunable

DOI: 10.1021/acs.jpcc.8b04019
J. Phys. Chem. C 2018, 122, 14846−14856

based on varying intermolecular interactions and ionic environments.

An important implication of pH-tunable diffusion relates to subsequent molecular orientation at the metal interface. Previous studies showed that slow diffusion or low molecular flux caused negatively charged molecules to adopt a larger molecular footprint on the metal surface thus minimizing its potential energy and surface density versus cases of high molecular flux.[4,23,36,72] To evaluate these effects on IE Ag@Au@SiO_2 nanoparticles, shifts in LSPR wavelength for samples equilibrated with 4-MBA are evaluated. To do this, the averaged λ_{max} values after initial adsorption occurs (i.e, incubation time larger than 30 min) as a function of pH are quantified. As shown in the inset of Figure 2A, the average λ_{max} for samples incubated in solution with pH near to or more acidic than the pK_a for 4-MBA are 572.5 nm versus ~571.5 nm in all higher pH solutions. In addition, the C−S stretching mode intensity collected using SERS is significantly smaller for the samples evaluated at pH 7.5 versus all other pH solutions. In its entirety, this suggests that molecular density is lower when adsorbed at the highest pH and higher when solutions are acidic, a trend directly related to molecular diffusion through the silica membrane and adsorption to the SERS active-interface.

pH and Intermolecular Interaction Effects on Aromatic Ring Stretching Vibrations. Raman signals depend on the magnitude of the induced dipole moment of molecules, which is a product of molecular polarizability and applied electric field.[81] While electromagnetic enhancement from the LSPR of plasmonic nanoparticles is the dominant mechanism for enhancement in SERS,[30,81−83] chemical enhancement also plays a role because of its dependence on the electron density of molecules.[33,84] For instance, pumping charge-transfer transitions in a molecule increases SERS signals via chemical enhancement.[31,32,85] Previous SERS studies using aromatic thiolates suggested that the asymmetric (b_2) and symmetric (a_1) C−C stretching modes are enhanced by charge-transfer and electromagnetic mechanisms,[23,31,32] respectively. As a result, relative changes in SERS intensities of these vibrational modes with increasing pH are analyzed using IE Ag@Au@SiO_2 nanoparticles so that pH-induced electron density variations in the molecules can be identified. Because electrons tend to localize in the aromatic rings of 4-MBA with increasing pH, chemical enhancement effects on SERS signals can be separated from the electromagnetic effects as these nanostructures are electromagnetically stable.

It is well-established that monolayer formation occurs in multiple steps including rapid adsorption followed by slow (i.e., 18+ hours) restructuring to reduce defect density in alkanethiol monolayers.[21,22,86] To identify impacts of intermolecular interactions upon initial adsorption, representative SERS spectra of 4-MBA at each pH after a 30 min incubation are shown in Figure 3A. Vibrational frequencies associated with C−S stretching (ν_{CS}, 1080 cm^{-1}), asymmetric C−C stretching ($\nu_{CC,as}$, 1582 cm^{-1}), and symmetric C−C stretching ($\nu_{CC,s}$, 1592 cm^{-1}) are observed. Relative SERS signals associated with asymmetric and symmetric C−C stretching modes (determined using curve fitting) with respect to the intensity at C−S stretching mode are shown in Figure 3B to evaluate chemical enhancement effects. Because the nanoparticles are electromagnetically stable, symmetric C−C stretching mode intensities exhibit no statistical difference when pH ranges from 4.5 to 6. As pH increases more, a slight

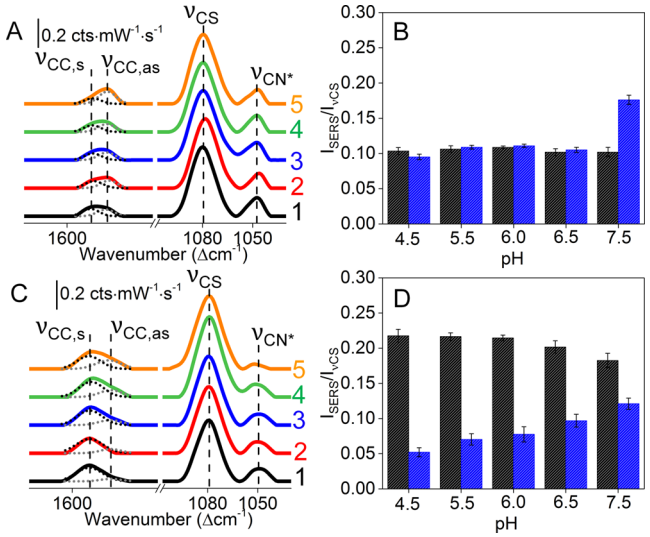

Figure 3. SERS spectra of 10 μM 4-MBA with 0.3 nM IE Ag@Au@SiO_2 nanoparticles at pH (1) 4.5, (2) 5.5, (3) 6.0, (4) 6.5, and (5) 7.5. (A) Representative spectra and (B) analysis are shown for 30 min incubations, while those for 18 h incubations are shown in panels C and D, respectively. All spectra are scaled to the C−S stretching mode intensity. Three vibrational modes are observed including C−S stretching (ν_{CS}, 1080 cm^{-1}), asymmetric C−C stretching ($\nu_{CC,as}$, 1582 cm^{-1}), and symmetric C−C stretching ($\nu_{CC,s}$, 1592 cm^{-1}). The peak of C−N stretching (ν_{CN}, 1048 cm^{-1}) is from silica. Representative curve fitting analyses for overlapping bands are indicated with dotted lines in panels A and C. Experimental conditions: Ag@Au@SiO_2 nanoparticles = 0.3 nM, 4-MBA = 10 μM, λ_{ex} = 785 nm, t_{int} = 10 s, P = 59 mW, 30 averages. The pH-dependent (black) symmetric and (blue) asymmetric C−C stretching mode intensities with respect to the C−S stretching intensity are shown after (B) 30 min and (D) 18 h. All SERS intensities obtained from 20 to 45 min are averaged.

decrease in the symmetric C−C stretch is observed and is consistent with an increase in molecular tilt angle with respect to the surface normal of Au (*vide infra*). In contrast, asymmetric C−C stretching mode intensities increase by 10% as pH increases from 4.5 to 6.5. At pH 7.5, the asymmetric mode increases by 50% and becomes more intense than the symmetric stretch.

To understand these observations, we build on the work by Hunter and Sanders[87] in which adjacent aromatic rings in an assembled monolayer[20,87] were treated as positively charged σ-frameworks sandwiched between negatively charged π-electron dense regions. In so doing, the interactions between adjacent aromatic rings were shown to represent a balance between electrostatic repulsive and van der Waal attractive interactions. We hypothesize that when molecular flux is high and because of the opposing forces described by Hunter and Sanders, electron density in the aromatic ring is reduced thus minimizing electrostatic repulsive and maximizing stabilizing attractive interactions. When molecular flux is low as when pH > pK_a, aromatic rings preferentially interact with the metal surface thus reducing the probability of $\pi-\pi$ stacking and dense monolayer formation. This effect is consistent with an increase in the electron density in the aromatic ring with increasing pH and an increase in chemical enhancement contributions.

This is further supported via analysis of the asymmetric (b_2) C−C stretching mode, which is expected to decrease with increasing $\pi-\pi$ interactions between aromatic rings. Because

DOI: 10.1021/acs.jpcc.8b04019
J. Phys. Chem. C 2018, 122, 14846−14856

$\pi-\pi$ interactions in a monolayer provide further stability once molecules adsorb, samples were allowed to equilibrate in 4-MBA at each pH for 18 h. Relative SERS signals for the asymmetric and symmetric C−C stretching modes with respect to the C−S stretching mode intensities are shown in Figure 3C,D. It is important to note that the SERS spectra collected at 18 h are different from those evaluated after 30 min of incubation with most notable differences in C−C asymmetric and symmetric stretching modes. For instance, the symmetric mode is ∼4 times larger than the asymmetric mode at pH 4.5. While the intensity for the asymmetric mode only slightly increases with increasing pH, the symmetric mode is always more intense than the asymmetric mode. We attribute these spectral variations versus data collected upon initial adsorption and pH to $\pi-\pi$ interaction differences between adsorbed 4-MBA molecules. As equilibration time increases, $\pi-\pi$ interactions between aromatic rings facilitate restructuring, which decreases the overall energy of the system and the relative chemical enhancement.

pH Effects, Intermolecular Interactions, and Carboxylic Acid Group Acidity. As discussed in the previous section, monolayer restructuring promotes $\pi-\pi$ interactions between adjacent aromatic rings thus reducing the electron density in the aromatic rings of 4-MBA. This is important because electron density in the aromatic ring impacts the acidity of any ring functional group and vice versa.[31,50,88,89] Previously, substituents were shown to induce π-electron delocalization thus reducing aromaticity and promoting $\pi-\pi$ interactions between two aromatic rings.[89] In particular, withdrawing functional groups substantially decreased electrostatic repulsions between neighboring aromatic rings and promoted $\pi-\pi$ stacking.[50,90] 4-MBA contains the electron-withdrawing carboxylate group; thus we hypothesize that the acidity of this group should be weakened upon monolayer formation and stabilization (i.e., pK_a should increase upon an increase in $\pi-\pi$ interactions between the aromatic rings in the monolayer). To evaluate the impact of $\pi-\pi$ interactions on the (Lewis) acidity of the carboxylate group as a function of pH and intermolecular interactions, vibrational frequencies associated with COOH stretching (ν_{COOH}, 693 cm^{-1})[36] and COO^- stretching (ν_{COO^-}, 848 cm^{-1})[71,72] modes are analyzed as a function of equilibration time.

Figure 4A shows representative SERS spectra of 4-MBA in the regions sensitive to the protonation state of COOH. In particular, spectra collected after initial adsorption at both pH 4.5 and 7.5 as well as after equilibration at pH 7.5 are shown as these represent the most dramatic spectral differences. Differences are noted. For instance, the COOH stretching mode intensity is smaller, while the COO^- mode is larger upon initial adsorption when incubated in pH 7.5 versus 4.5. This difference is attributed to the pH dependent fraction of deprotonated 4-MBA molecules available for adsorption as controlled by flux through the silica membrane. To quantify this spectral variation in terms of protonated and deprotonated molecules, a relative ratio (R) is calculated as follows:

$$R = \frac{I_{COOH} - I_{COO^-}}{I_{COOH} + I_{COO^-}} \quad (5)$$

where I_{COOH} and I_{COO^-} are intensities of the COOH and COO^- stretching modes, respectively. By plotting these data as a function of pH, a response consistent with a modified Henderson−Hasselbalch model is observed (Figure 4B).

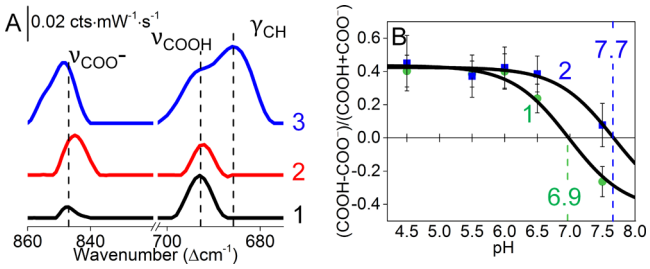

Figure 4. (A) SERS spectra of 4-MBA at (1) pH 4.5 after 30 min, (2) pH 7.5 after 30 min, and (3) pH 7.5 after 18 h. Vibrational modes are COOH stretching (ν_{COOH}, 693 cm^{-1}), COO^- stretching (ν_{COO^-}, 848 cm^{-1}), and CH out-of-plane bending (γ_{CH}, 684 cm^{-1}). Experimental conditions: Ag@Au@SiO_2 nanoparticles = 0.3 nM, 4-MBA = 10 μM, λ_{ex}= 785 nm, t_{int}= 10 s, P = 59 mW, averages = 30. (B) The $\frac{I_{COOH} - I_{COO^-}}{I_{COOH} + I_{COO^-}}$ ratio determined from experimental data after incubation times of (1) 30 min and (2) 18 h. The lines represent modified Henderson−Hasselbalch equilibria, and a zero-crossing point is used to estimate the surface pK_a of 4-MBA, which is 6.9 and 7.7 after 30 min and 18 h, respectively.

Furthermore, the inflection point of this curve can be used to indicate the surface pK_a of the carboxylic group. From this analysis, the effective pK_a of the carboxylic acid group is 6.9 upon initial adsorption. This finding indicates that at pH ∼ 6.5 or higher, the fraction of deprotonated molecules, which exhibit greater tilt angles with respect to the surface normal, increases thus causing a decrease in the symmetric C−C stretching mode as observed in Figure 3A,B.

If intermolecular interactions from $\pi-\pi$ interactions induce more electron density into the carboxylic acid group, monolayer restructuring should cause the surface pK_a to become less acidic. To evaluate this effect, SERS spectra were collected at each pH, and samples were allowed to equilibrate for 18 h. A comparison of the data collected at pH 7.5 after 0.5 and 18 h is shown in Figure 4A-2,A-3, respectively. Significant differences are noted. First, both modes associated with the carboxylic acid group increase in intensity. Second, the carboxylate vibrational mode blue-shifts by ∼2 cm^{-1} as incubation time increases and the monolayer becomes more ordered. Finally, the out-of-plane C−H bending mode (γ_{CH})[31] is observed at 684 cm^{-1} at pH 7.5 and long incubation times. These spectral variations are consistent with a change in fraction of protonated to deprotonated carboxylic acid groups, intermolecular interactions, and molecular orientation with respect to the surface normal.

To more clearly identify these observations, the relative ratio of protonated and deprotonated functional groups are assessed from pH dependent SERS spectra collected after 18 h. As shown in Figure 4B-2, data collected at the most acidic pHs are identical to those collected upon initial adsorption. As solution pH approaches the pK_a of the carboxylic acid group, deviations are noted. As such, the effective pK_a is 7.7, a value 0.8 pH units less acidic than estimated from initial adsorption data. This result suggests that the acidity of the carboxylic acid functional group on the aromatic ring is weakening and further supports the assertion that monolayer restructuring, which occurs over time via $\pi-\pi$ interaction stabilization causes the electrons in the aromatic ring to become delocalized (into the electron withdrawing functional group) thus impacting acidity. A similar response was previously observed for cyclophanes where $\pi-\pi$ interactions and subsequent charge delocalization

DOI: 10.1021/acs.jpcc.8b04019
J. Phys. Chem. C 2018, 122, 14846−14856

were promoted when the distance between two rings decreased.[90,91] In the present case, an increase in electron density in the carboxylic acid groups likely limits its electron accepting ability thus weakening its acidity. Because monolayer restructuring reduces the electron density in aromatic rings, the decrease in 4-MBA acidity can be correlated to a reduction in the vibrational modes sensitive to chemical enhancement.

In order to illustrate the effect of electron delocalization from the ring with the acidity of carboxylic acid groups, potential energies are calculated using three protonated benzoic acid molecules aligned via their aromatic rings with separation distances ranging from 0.33 to 0.42 nm to mimic the packing density of 4-MBA on gold. These intermolecular distances were determined from previous studies in which $\pi-\pi$ interactions between aromatic rings ranged from 0.33 to 0.38 nm.[49−51] These results are summarized in Figure 5A where the molecular structure of protonated acid is shown. Potential energies at the O and H atoms are most sensitive to acidity and further analyzed. Figure 5B reveals that as intermolecular distance decreases from 0.42 to 0.33 nm, the potentials at the O and H atoms become more negative and less positive, respectively. This increase in electron density in the carboxylic acid groups is consistent with the promotion of electron delocalization from the aromatic rings to carboxylic groups, a phenomenon similar to what is predicted by SERS.

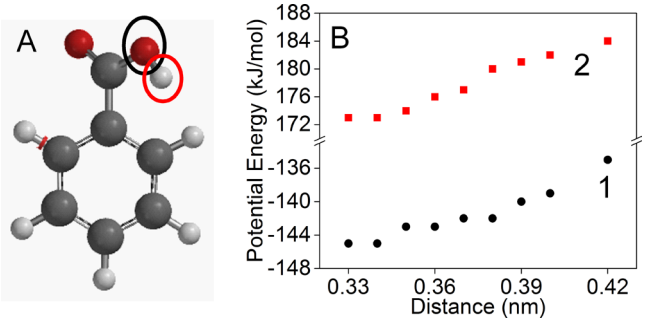

Figure 5. (A) Molecular model of an aromatic carboxylic acid containing molecule. Atoms involved in acidity are circled in either black or red to indicate involved O and H atoms in the carboxylic acid, respectively. (B) Calculated electrostatic potential energy of (1) O and (2) H atoms as a function of intermolecular separation distance between aromatic rings.

Effects of intermolecular interactions and monolayer restructuring are not limited to carboxylic acid groups only but also to the C−H groups on the aromatic ring. Previously, it was demonstrated that the out-of-plane CH bending mode (γ_{CH}, 684 cm^{-1}) was sensitive to molecular orientation[23] (i.e., increase in tilt angle) and to π-electron delocalization.[31] As shown in Figure 4A-3, this vibrational mode is observed at all pH's after a long incubation (18 h). As the monolayer becomes more ordered via favorable $\pi-\pi$ interactions,[92,93] the aromatic rings become more tilted and electrons in aromatic rings delocalize to the carboxylic acid and CH groups. Consequently, the enhancement of this mode is promoted because of an increase in the Raman cross-section of this mode via surface selection rules (electromagnetic enhancement) and an increase in polarizability (chemical enhancement).

CONCLUSIONS

In summary, this study revealed how Ag@Au nanoparticles electromagnetically stabilized by microporous silica membranes can be used to control the local pH near, mass transfer of molecules to, and intermolecular interactions between molecules on the metal. Intermolecular interactions and their associated energetics influence what and how many molecules adsorb to the metal surface. This was analyzed using LSPR and SERS. First, effective molecular diffusion coefficients were calculated using Fick's second law of diffusion and shown to depend on the fraction of protonated molecules in solution as well as near the silica membrane. Molecular flux decreased as the fraction of deprotonated molecules near the silica interface increased, which depended on pH. Second, LSPR and SERS analysis of the C−S stretching mode indicated that these differences in flux influenced the number of molecules on the metal surface whereby higher flux led to more molecules binding to the metal surface. At the highest pH, low molecular flux caused 4-MBA to maximize its surface footprint thus reducing the molecular density in the monolayer. Third, monolayer restructuring via $\pi-\pi$ interactions between the aromatic molecules caused the electron density in the aromatic rings to decrease thus causing vibrational modes that are sensitive to chemical enhancement to decrease. These interactions also caused the electron density in carboxylic acid groups to increase. Consequently, the COO−H bond was strengthened and the acidity of the functional group weakened thereby increasing its pK_a from 4.79 to 6.9. Finally, monolayer restructuring was promoted through longer equilibration times and $\pi-\pi$ interaction stabilization, which further decreased the acidity of the carboxylic acid group to a pK_a of 7.7. All in all, this study highlights the importance of how simple parameters (solution pH or incubation time) can influence the observed SERS signals of small molecules via chemical enhancement mechanism. Future studies should carefully consider these when reporting and interpreting SERS spectral data.

ASSOCIATED CONTENT

Supporting Information

The Supporting Information is available free of charge on the ACS Publications website at DOI: 10.1021/acs.jpcc.8b04019.

LSPR spectra of internally etched Ag@Au@SiO_2 nanoparticles at varying pH (PDF)

AUTHOR INFORMATION

Corresponding Author

*Phone: (319) 384-3695. Fax (319) 335-1270. E-mail: amanda-haes@uiowa.edu.

ORCID

Amanda J. Haes: 0000-0001-7232-6825

Notes

The authors declare no competing financial interest.

ACKNOWLEDGMENTS

This work was funded by the National Science Foundation (CHEM-1707859 and CHEM-1150135).

REFERENCES

(1) Dendisova-Vyskovska, M.; Kokaislova, A.; Oncak, M.; Matejka, P. SERS and in Situ SERS Spectroscopy of Riboflavin Adsorbed on Silver, Gold and Copper Substrates. Elucidation of Variability of Surface Orientation Based on Both Experimental and Theoretical Approach. *J. Mol. Struct.* **2013**, *1038*, 19−28.

(2) Shrestha, B. K.; Haes, A. J. Improving Surface Enhanced Raman Signal Reproducibility Using Gold-Coated Silver Nanospheres Encapsulated in Silica Membranes. *J. Opt.* **2015**, *17*, 114017.
(3) Khurana, P.; Thatai, S.; Prasad, S.; Soni, S.; Kumar, D. Ag_{core}–Au_{shell} Bimetallic Nanocomposites: Gold Shell Thickness Dependent Study for SERS Enhancement. *Microchem. J.* **2016**, *124*, 819–823.
(4) Lu, G.; Shrestha, B.; Haes, A. J. Importance of Tilt Angles of Adsorbed Aromatic Molecules on Nanoparticle Rattle SERS Substrates. *J. Phys. Chem. C* **2016**, *120*, 20759–20767.
(5) Goddard, G.; Brown, L. O.; Habbersett, R.; Brady, C. I.; Martin, J. C.; Graves, S. W.; Freyer, J. P.; Doorn, S. K. High Resolution Spectral Analysis of Individual SERS-Active Nanoparticles in Flow. *J. Am. Chem. Soc.* **2010**, *132*, 6081–6090.
(6) Jacobs, K. T.; Schultz, Z. D. Increased SERS Detection Efficiency for Characterizing Rare Events in Flow. *Anal. Chem.* **2015**, *87*, 8090–8095.
(7) Taylor, A. B.; Zijlstra, P. Single-Molecule Plasmon Sensing: Current Status and Future Prospects. *ACS Sensors* **2017**, *2*, 1103–1122.
(8) Kolomeisky, A. B.; Uppulury, K. How Interactions Control Molecular Transport In channels. *J. Stat. Phys.* **2011**, *142*, 1268–1276.
(9) Zilman, A. Effects of Multiple Occupancy and Interparticle Interactions on Selective Transport through Narrow Channels: Theory Versus Experiment. *Biophys. J.* **2009**, *96*, 1235–1248.
(10) Berezhkovskii, A. M.; Pustovoit, M. A.; Bezrukov, S. M. Channel-Facilitated Membrane Transport: Transit Probability and Interaction with the Channel. *J. Chem. Phys.* **2002**, *116*, 9952–9956.
(11) Berezhkovskii, A. M.; Pustovoit, M. A.; Bezrukov, S. M. Channel-Facilitated Membrane Transport:Average Lifetimes in the Channel. *J. Chem. Phys.* **2003**, *119*, 3943–3951.
(12) Bauer, W. R.; Nadler, W. Thermodynamics of Competitive Molecular Channel Transport: Application to Artificial Nuclear Pores. *PLoS One* **2010**, *5*, e15160.
(13) Agah, S.; Pasquali, M.; Kolomeisky, A. B. Theoretical Analysis of Selectivity Mechanisms in Molecular Transport through Channels and Nanopores. *J. Chem. Phys.* **2015**, *142*, 044705.
(14) Kolomeisky, A. B. Channel-Facilitated Molecular Transport across Membranes: Attraction, Repulsion, and Asymmetry. *Phys. Rev. Lett.* **2007**, *98*, 048105.
(15) Zilman, A.; Di Talia, S.; Jovanovic-Talisman, T.; Chait, B. T.; Rout, M. P.; Magnasco, M. O. Enhancement of Transport Selectivity through Nano-Channels by Non-Specific Competition. *PLoS Comput. Biol.* **2010**, *6*, e1000804.
(16) Danelon, C.; Brando, T.; Winterhalter, M. Probing the Orientation of Reconstituted Maltoporin Channels at the Single-Protein Level. *J. Biol. Chem.* **2003**, *278*, 35542–35551.
(17) Wolfe, A. J.; Mohammad; Cheley, S.; Bayley, H.; Movileanu, L. Catalyzing the Translocation of Polypeptides through Attractive Interactions. *J. Am. Chem. Soc.* **2007**, *129*, 14034–14041.
(18) Mohammad; Prakash, S.; Matouschek, A.; Movileanu, L. Controlling a Single Protein in a Nanopore through Electrostatic Traps. *J. Am. Chem. Soc.* **2008**, *130*, 4081–4088.
(19) Chacinska, A.; Pfanner, N.; Meisinger, C. How Mitochondria Import Hydrophilic and Hydrophobic Proteins. *Trends Cell Biol.* **2002**, *12*, 299–303.
(20) Hsu, S.-H.; Reinhoudt, D. N.; Huskens, J.; Velders, A. H. Lateral Interactions at Functional Monolayers. *J. Mater. Chem.* **2011**, *21*, 2428–2444.
(21) Love, J. C.; Estroff, L. A.; Kriebel, J. K.; Nuzzo, R. G.; Whitesides, G. M. Self-Assembled Monolayers of Thiolates on Metals as a Form of Nanotechnology. *Chem. Rev.* **2005**, *105*, 1103–1170.
(22) Schwartz, D. K. Mechanisms and Kinetics of Self-Assembled Monolayer Formation. *Annu. Rev. Phys. Chem.* **2001**, *52*, 107–137.
(23) Wang, X.; Zhong, J.-H.; Zhang, M.; Liu, Z.; Wu, D.-Y.; Ren, B. Revealing Intermolecular Interaction and Surface Restructuring of an Aromatic Thiol Assembling on Au(111) by Tip-Enhanced Raman Spectroscopy. *Anal. Chem.* **2016**, *88*, 915–921.
(24) Ivanov, M. R.; Bednar, H. R.; Haes, A. J. Investigations of the Mechanism of Gold Nanoparticle Stability and Surface Functionalization in Capillary Electrophoresis. *ACS Nano* **2009**, *3*, 386–394.
(25) Pienpinijtham, P.; Vantasin, S.; Kitahama, Y.; Ekgasit, S.; Ozaki, Y. Nanoscale pH Profile at a Solution/Solid Interface by Chemically Modified Tip-Enhanced Raman Scattering. *J. Phys. Chem. C* **2016**, *120*, 14663–14668.
(26) Kneipp, J.; Kneipp, H.; Wittig, B.; Kneipp, K. Following the Dynamics of pH in Endosomes of Live Cells with SERS Nanosensors. *J. Phys. Chem. C* **2010**, *114*, 7421–7426.
(27) Jaworska, A.; Jamieson, L. E.; Malek, K.; Campbell, C. J.; Choo, J.; Chlopicki, S.; Baranska, M. SERS-Based Monitoring of the Intracellular pH in Endothelial Cells: The Influence of the Extracellular Environment and Tumour Necrosis Factor-α. *Analyst* **2015**, *140*, 2321–2329.
(28) Pallaoro, A.; Braun, G. B.; Reich, N. O.; Moskovits, M. Mapping Local pH in Live Cells Using Encapsulated Fluorescent SERS Nanotags. *Small* **2010**, *6*, 618–622.
(29) Xi, W.; Shrestha, B. K.; Haes, A. J. Promoting Intra- and Intermolecular Interactions in Surface-Enhanced Raman Scattering. *Anal. Chem.* **2018**, *90*, 128–143.
(30) Schatz, G. C.; Van Duyne, R. P. Electromagnetic Mechanism of Surface-Enhanced Spectroscopy. In *Handbook of Vibrational Spectroscopy*; John Wiley & Sons, Ltd: 2006.
(31) Wang, Y.; Ji, W.; Sui, H.; Kitahama, Y.; Ruan, W.; Ozaki, Y.; Zhao, B. Exploring the Effect of Intermolecular H-Bonding: A Study on Charge-Transfer Contribution to Surface-Enhanced Raman Scattering of p-Mercaptobenzoic Acid. *J. Phys. Chem. C* **2014**, *118*, 10191–10197.
(32) Yoon, J. H.; Park, J. S.; Yoon, S. Time-Dependent and Symmetry-Selective Charge-Transfer Contribution to Sers in Gold Nanoparticle Aggregates. *Langmuir* **2009**, *25*, 12475–12480.
(33) Lombardi, J. R.; Birke, R. L.; Lu, T.; Xu, J. Charge-Transfer Theory of Surface Enhanced Raman Spectroscopy: Herzberg–Teller Contributions. *J. Chem. Phys.* **1986**, *84*, 4174–4180.
(34) Jensen, L.; Aikens, C. M.; Schatz, G. C. Electronic Structure Methods for Studying Surface-Enhanced Raman Scattering. *Chem. Soc. Rev.* **2008**, *37*, 1061–1073.
(35) Ru, E. L.; Etchegoin, P. *Principles of Surface-Enhanced Raman Spectroscopy and Related Plasmonic Effects*; Elsevier Science: 2008.
(36) Guhlke, M.; Heiner, Z.; Kneipp, J. Combined near-Infrared Excited SEHRS and SERS Spectra of pH Sensors Using Silver Nanostructures. *Phys. Chem. Chem. Phys.* **2015**, *17*, 26093–26100.
(37) Cui, Y.; Ren, B.; Yao, J.-L.; Gu, R.-A.; Tian, Z.-Q. Synthesis of Ag_{core}-Au_{shell} Bimetallic Nanoparticles for Immunoassay Based on Surface-Enhanced Raman Spectroscopy. *J. Phys. Chem. B* **2006**, *110*, 4002–4006.
(38) Srnova-Sloufova, I.; Vlckova, B.; Bastl, Z.; Hasslett, T. L. Bimetallic (Ag)Au Nanoparticles Prepared by the Seed Growth Method: Two-Dimensional Assembling, Characterization by Energy Dispersive X-Ray Analysis, X-Ray Photoelectron Spectroscopy, and Surface Enhanced Raman Spectroscopy, and Proposed Mechanism of Growth. *Langmuir* **2004**, *20*, 3407–3415.
(39) Paramelle, D.; Sadovoy, A.; Gorelik, S.; Free, P.; Hobley, J.; Fernig, D. G. A Rapid Method to Estimate the Concentration of Citrate Capped Silver Nanoparticles from UV-Visible Light Spectra. *Analyst* **2014**, *139*, 4855–4861.
(40) Roca, M.; Haes, A. J. Silica-Void-Gold Nanoparticles: Temporally Stable Surface-Enhanced Raman Scattering Substrates. *J. Am. Chem. Soc.* **2008**, *130*, 14273–14279.
(41) Liz-Marzán, L. M.; Giersig, M.; Mulvaney, P. Synthesis of Nanosized Gold–Silica Core–Shell Particles. *Langmuir* **1996**, *12*, 4329–4335.
(42) Stöber, W.; Fink, A.; Bohn, E. Controlled Growth of Monodisperse Silica Spheres in the Micron Size Range. *J. Colloid Interface Sci.* **1968**, *26*, 62–69.
(43) Pierre, M. C. S.; Haes, A. J. Purification Implications on SERS Activity of Silica Coated Gold Nanospheres. *Anal. Chem.* **2012**, *84*, 7906–7911.

DOI: 10.1021/acs.jpcc.8b04019
J. Phys. Chem. C 2018, 122, 14846–14856

(44) Delgado, A. V.; González-Caballero, F.; Hunter, R. J.; Koopal, L. K.; Lyklema, J. Measurement and Interpretation of Electrokinetic Phenomena. *J. Colloid Interface Sci.* **2007**, *309*, 194−224.
(45) Hunter, R. J. *Zeta Potential in Colloid Science: Principles and Applications*; Academic Press: London, 1981.
(46) Mullen, K. I.; Wang, D.; Crane, L. G.; Carron, K. T. Determination of pH with Surface-Enhanced Raman Fiber Optic Probes. *Anal. Chem.* **1992**, *64*, 930−936.
(47) Volkert, A. A.; Pierre, M. C. S.; Shrestha, B.; Haes, A. J. Implications of Sample Aging on the Formation of Internally Etched Silica Coated Gold Nanoparticles. *RSC Adv.* **2015**, *5*, 3774−3780.
(48) Haes, A. J.; Zou, S.; Schatz, G. C.; Van Duyne, R. P. Nanoscale Optical Biosensor: Short Range Distance Dependence of the Localized Surface Plasmon Resonance of Noble Metal Nanoparticles. *J. Phys. Chem. B* **2004**, *108*, 6961−6968.
(49) Janiak, C. A Critical Account on π-π Stacking in Metal Complexes with Aromatic Nitrogen-Containing Ligands. *J. Chem. Soc., Dalton Trans.* **2000**, 3885−3896.
(50) Zhao, R.; Zhang, R.-Q. A New Insight into π-π Stacking Involving Remarkable Orbital Interactions. *Phys. Chem. Chem. Phys.* **2016**, *18*, 25452−25457.
(51) Alvarez, S. A Cartography of the Van Der Waals Territories. *Dalton Trans.* **2013**, *42*, 8617−8636.
(52) Liu, X.; Vlugt, T. J. H.; Bardow, A. Predictive Darken Equation for Maxwell-Stefan Diffusivities in Multicomponent Mixtures. *Ind. Eng. Chem. Res.* **2011**, *50*, 10350−10358.
(53) Sridhar, S. A Commentary on "Diffusion, Mobility and Their Interrelation through Free Energy in Binary Metallic Systems," L.S. Darken: Trans. AIME, 1948, vol. 175, p. 184ff. *Metall. Mater. Trans. A* **2010**, *41*, 543−562.
(54) Smith, W. F.; Hashemi, J. *Foundations of Materials Science and Engineering*, 4th ed.; McGraw-Hill: Boston, 2005.
(55) Dreaden, E. C.; Austin, L. A.; Mackey, M. A.; El-Sayed, M. A. Size Matters: Gold Nanoparticles in Targeted Cancer Drug Delivery. *Ther. Delivery* **2012**, *3*, 457−478.
(56) Burgi, T. Properties of the Gold-Sulphur Interface: From Self-Assembled Monolayers to Clusters. *Nanoscale* **2015**, *7*, 15553−15567.
(57) Ulman, A. Formation and Structure of Self-Assembled Monolayers. *Chem. Rev.* **1996**, *96*, 1533−1554.
(58) Noulty, R. A.; Leaist, D. G. Diffusion Coefficient of Aqueous Benzoic Acid at 25.Degree.C. *J. Chem. Eng. Data* **1987**, *32*, 418−420.
(59) Kievsky, Y. Y.; Carey, B.; Naik, S.; Mangan, N.; ben-Avraham, D.; Sokolov, I. Dynamics of Molecular Diffusion of Rhodamine 6G in Silica Nanochannels. *J. Chem. Phys.* **2008**, *128*, 151102.
(60) Yamaguchi, A.; Mekawy, M. M.; Chen, Y.; Suzuki, S.; Morita, K.; Teramae, N. Diffusion of Metal Complexes inside of Silica−Surfactant Nanochannels within a Porous Alumina Membrane. *J. Phys. Chem. B* **2008**, *112*, 2024−2030.
(61) Rivera, D.; Harris, J. M. In Situ Atr-Ft-Ir Kinetic Studies of Molecular Transport and Surface Binding in Thin Sol−Gel Films: Reactions of Chlorosilane Reagents in Porous Silica Materials. *Anal. Chem.* **2001**, *73*, 411−423.
(62) Ruthven, D. M. *Principles of Adsorption and Adsorption Processes*; Wiley: 1984.
(63) Tansub, W.; Tuitemwong, K.; Limsuwan, P.; Theparoonrat, S.; Tuitemwong, P. Synthesis of Antibodies-Conjugated Fluorescent Dye-Doped Silica Nanoparticles for a Rapid Single Step Detection of Campylobacter Jejuni in Live Poultry. *J. Nanomater.* **2012**, *2012*, 865186.
(64) Riegel, B.; Kiefer, W.; Hofacker, S.; Schottner, G. FT-Raman-Spectroscopic Investigations of the System Glycidoxypropyltrimethoxysilane/Aminopropyltriethoxysilane. *J. Sol-Gel Sci. Technol.* **1998**, *13*, 385−390.
(65) Posset, U.; Lankers, M.; Kiefer, W.; Steins, H.; Schottner, G. Polarized Raman Spectra from Some Sol-Gel Precursors and Micro-Raman Study of One Selected Copolymer. *Appl. Spectrosc.* **1993**, *47*, 1600−1603.
(66) Mosier-Boss, P. A. Review of SERS Substrates for Chemical Sensing. *Nanomaterials* **2017**, *7*, 142.
(67) Inscore, F. E.; Gift, A. D.; Maksymiuk, P.; Farquharson, S. Characterization of Chemical Warfare G-Agent Hydrolysis Products by Surface-Enhanced Raman Spectroscopy. *Proc. SPIE* **2004**, *5585*, 46−52.
(68) Tripp, R. A.; Dluhy, R. A.; Zhao, Y. Novel Nanostructures for SERS Biosensing. *Nano Today* **2008**, *3*, 31−37.
(69) Stewart, S.; Fredericks, P. M. Surface-Enhanced Raman Spectroscopy of Peptides and Proteins Adsorbed on an Electrochemically Prepared Silver Surface. *Spectrochim. Acta, Part A* **1999**, *55*, 1615−1640.
(70) Bao, P.-D.; Huang, T.-Q.; Liu, X.-M.; Wu, T.-Q. Surface-Enhanced Raman Spectroscopy of Insect Nuclear Polyhedrosis Virus. *J. Raman Spectrosc.* **2001**, *32*, 227−230.
(71) Lee, S. B.; Kim, K.; Kim, M. S. Surface-Enhanced Raman Scattering of o-Mercaptobenzoic Acid in Silver Sol. *J. Raman Spectrosc.* **1991**, *22*, 811−817.
(72) Michota, A.; Bukowska, J. Surface-Enhanced Raman Scattering (SERS) of 4-Mercaptobenzoic Acid on Silver and Gold Substrates. *J. Raman Spectrosc.* **2003**, *34*, 21−25.
(73) Ma, C.; Harris, J. M. Surface-Enhanced Raman Spectroscopy Investigation of the Potential-Dependent Acid−Base Chemistry of Silver-Immobilized 2-Mercaptobenzoic Acid. *Langmuir* **2011**, *27*, 3527−3533.
(74) Liu, Y.; Yuan, H.; Fales, A. M.; Vo-Dinh, T. Ph-Sensing Nanostar Probe Using Surface-Enhanced Raman Scattering (SERS): Theoretical and Experimental Studies. *J. Raman Spectrosc.* **2013**, *44*, 980−986.
(75) Kim, K.-M.; Kim, H. M.; Lee, W.-J.; Lee, C.-W.; Kim, T.-i.; Lee, J.-K.; Jeong, J.; Paek, S.-M.; Oh, J.-M. Surface Treatment of Silica Nanoparticles for Stable and Charge-Controlled Colloidal Silica. *Int. J. Nanomed.* **2014**, *9*, 29−40.
(76) Park, S.; Lee, H.-B. Effect of pH on Monolayer Properties of Colloidal Silica Particles at the Air/Water Interface. *Colloid Polym. Sci.* **2012**, *290*, 445−455.
(77) Karabacak, R. B.; Türk, H. Preparation of PS Colloids with DMA and MMA Comonomers and Suitability of P(S/DMA) for Colloidal Silica Deposition. *J. Macromol. Sci., Part A: Pure Appl.Chem.* **2012**, *49*, 680−688.
(78) Yuan, J.-J.; Mykhaylyk, O. O.; Ryan, A. J.; Armes, S. P. Cross-Linking of Cationic Block Copolymer Micelles by Silica Deposition. *J. Am. Chem. Soc.* **2007**, *129*, 1717−1723.
(79) Hiramatsu, H.; Osterloh, F. E. pH-Controlled Assembly and Disassembly of Electrostatically Linked CdSe−SiO_2 and Au−SiO_2 Nanoparticle Clusters. *Langmuir* **2003**, *19*, 7003−7011.
(80) Wei, H.; Willner, M. R.; Marr, L. C.; Vikesland, P. J. Highly Stable SERS pH Nanoprobes Produced by Co-Solvent Controlled Aunp Aggregation. *Analyst* **2016**, *141*, 5159−5169.
(81) Xia, Y.; Campbell, D. J. Plasmons: Why Should We Care? *J. Chem. Educ.* **2007**, *84*, 91−96.
(82) Haes, A. J.; Haynes, C. L.; McFarland, A. D.; Schatz, G. C.; Van Duyne, R. P.; Zou, S. Plasmonic Materials for Surface-Enhanced Sensing and Spectroscopy. *MRS Bull.* **2005**, *30*, 368−375.
(83) Willets, K. A.; Van Duyne, R. P. Localized Surface Plasmon Resonance Spectroscopy and Sensing. *Annu. Rev. Phys. Chem.* **2007**, *58*, 267−297.
(84) Campion, A.; Ivanecky, J. E.; Child, C. M.; Foster, M. On the Mechanism of Chemical Enhancement in Surface-Enhanced Raman Scattering. *J. Am. Chem. Soc.* **1995**, *117*, 11807−11808.
(85) Chowdhury, J. How the Charge Transfer (CT) Contributions Influence the SERS Spectra of Molecules? A Retrospective from the View of Albrecht's "A" and Herzberg-Teller Contributions. *Appl. Spectrosc. Rev.* **2015**, *50*, 240−260.
(86) Asiaei, S.; Nieva, P.; Vijayan, M. M. Fast Kinetics of Thiolic Self-Assembled Monolayer Adsorption on Gold: Modeling and Confirmation by Protein Binding. *J. Phys. Chem. B* **2014**, *118*, 13697−13703.
(87) Hunter, C. A.; Sanders, J. K. M. The Nature of π-π Interactions. *J. Am. Chem. Soc.* **1990**, *112*, 5525−5534.

DOI: 10.1021/acs.jpcc.8b04019
J. Phys. Chem. C 2018, 122, 14846−14856

(88) Wheeler, S. E. Understanding Substituent Effects in Noncovalent Interactions Involving Aromatic Rings. *Acc. Chem. Res.* **2013**, *46*, 1029−1038.
(89) Bloom, J. W. G.; Wheeler, S. E. Taking the Aromaticity out of Aromatic Interactions. *Angew. Chem., Int. Ed.* **2011**, *50*, 7847−7849.
(90) Fujitsuka, M.; Cho, D. W.; Tojo, S.; Yamashiro, S.; Shinmyozu, T.; Majima, T. Transannular Distance Dependence of Stabilization Energy of the Intramolecular Dimer Radical Cation of Cyclophanes. *J. Phys. Chem. A* **2006**, *110*, 5735−5739.
(91) Fujitsuka, M.; Tojo, S.; Shibahara, M.; Watanabe, M.; Shinmyozu, T.; Majima, T. Delocalization of Positive Charge in π-Stacked Multi-Benzene Rings in Multilayered Cyclophanes. *J. Phys. Chem. A* **2011**, *115*, 741−746.
(92) Hunter, C. A.; Lawson, K. R.; Perkins, J.; Urch, C. J. Aromatic Interactions. *Perk. Trans.* **2001**, *2*, 651−669.
(93) Matthews, R. P.; Welton, T.; Hunt, P. A. Competitive π Interactions and Hydrogen Bonding within Imidazolium Ionic Liquids. *Phys. Chem. Chem. Phys.* **2014**, *16*, 3238−3253.

DOI: 10.1021/acs.jpcc.8b04019
J. Phys. Chem. C 2018, 122, 14846−14856